The Sedimentation of Papermaking Fibers

E. W. K. Young, D. M. Martinez, and J. A. Olson
Pulp and Paper Centre, University of British Columbia, Vancouver, British Columbia V6T 1Z4, Canada

K. Buckley, S. Jivan, and T. J. Ruth
TRIUMF, University of British Columbia, Vancouver, British Columbia V6T 2A3, Canada

V. Sossi
Dept. of Physics and Astronomy, University of British Columbia, Vancouver, British Columbia V6T 1Z1, Canada

DOI 10.1002/aic.10902

The motion of ^{18}F radioactively labeled papermaking fibers settling in the midst of a suspension of nonradioactive fibers has been studied using positron emission tomography (PET). Various fractions were separated from the whole-pulp suspension, radioactively labeled, and reintroduced into the original suspension. Tracer concentration profiles were measured dynamically throughout the sedimenting structure over the first 2 h of settling. These profiles were then used in conjunction with the Eulerian volume-averaged two-phase flow equations to estimate the permeability and solid-phase stress functions for this suspension. Good agreement was found between the experimental data and the numerical model using particular functional forms for permeability and solid stress. The general approach outlined here can be used to examine the networking characteristics of different mixed suspensions of fibers. © 2006 American Institute of Chemical Engineers *AIChE J,* 52: 2697–2706, 2006

Introduction

In the simplest terms, paper is manufactured by filtering a dilute suspension of cellulose fibers. Under normal processing conditions, these suspensions aggregate naturally into flocs or clumps that possess measurable strength. Fiber flocculation is a deleterious effect as it creates paper that appears cloudy or grainy when examined in light. Indeed, graininess affects the aesthetic quality of the paper, especially when printed on, and influences mechanical properties such as tensile strength.[1,2]

As paper quality is closely related to flocculation, it is useful to gain a deeper understanding of the particle dispersion (mixing) or clumping (flocculation) mechanisms. There are a number of studies found in the literature that consider sedimentation as a means of understanding these mechanisms.[3-11] In general these studies examine settling in the Stokes' regime, with dilute suspensions, and focus on understanding the long-range hydrodynamic interactions that lead to flocculation. Although in some ways the pulp dewatering process is different from sedimentation, these studies generally still reveal important physical aspects of the fiber network formation process.

At concentrations relevant to papermaking, many authors consider the suspension to behave like a continuum,[12,13] and express the transport of mass and momentum using the Eulerian volume-averaged two-phase flow equations.[12-15] This approach constitutes the focus of the current work. Rearranging this set of fundamental equations leads to a momentum balance dependent on gravity, solid and fluid stresses, and an interphase momentum transfer term, all of which can be modeled using empirical relationships. As expressed by Concha et al.[16] for related sedimenting suspensions, the equations of motion reduce to

---

E. W. K. Young and J. A. Olson are also affiliated with the Dept. of Mechanical Engineering, University of British Columbia and D. M. Martinez is also affiliated with the Dept. of Chemical and Biological Engineering, University of British Columbia, Vancouver, British Columbia V6T 1Z4, Canada.
Correspondence concerning this article should be addressed to E. W. K. Young at edmyoung@gmail.com.

$$\frac{\partial \phi}{\partial t} - \frac{\partial}{\partial y}\left[\frac{\Delta\rho g \phi^2 k(\phi)}{\mu}\right] = \frac{\partial}{\partial y}\left[\frac{\phi k(\phi)\sigma_e'(\phi)}{\mu}\frac{\partial \phi}{\partial y}\right] \quad (1)$$

$$\phi[h(0), t] = 0 \qquad \text{for } t > 0 \quad (2)$$

$$\left.\frac{\partial \phi}{\partial y}\right|_{y=0} = \left.\frac{\Delta\rho\phi g}{\sigma_e'(\phi)}\right|_{y=0} \qquad \text{if } \phi(0, t) \geq \phi_g \quad (3)$$

$$\left.\frac{\partial \phi}{\partial y}\right|_{y=h(t)} = \left.\left[-\frac{\mu}{k(\phi)\sigma_e'(\phi)}\frac{dh}{dt} - \frac{\Delta\rho\phi g}{\sigma_e'(\phi)}\right]\right|_{y=h(t)} \quad (4)$$

$$\phi_0 H_0 = \int_{y=0}^{y=h(t)} \phi(y, t)dy \quad (5)$$

In the above equations, $\phi = \phi(y, t)$ is the volume fraction of fibers, whereas ϕ_0 is the initial fiber volume fraction, constant along the entire initial height of the suspension H_0; y is the vertical distance above the bottom of the column; $\Delta\rho$ is the difference in densities between the fiber and the fluid; g is the acceleration arising from gravity; μ is the fluid viscosity; $k(\phi)$ is the permeability; $\sigma_e(\phi)$ represents the solid-stress function of the network; and $h(t)$ is the elevation of the interface between the suspension and the clear fluid. The primed symbol represents differentiation with respect to ϕ. Equation 1 assumes that the Reynolds number is small, the solid- and fluid-phase inertial terms and the shear stress terms are small compared to the other terms, and the fibers do not deform significantly under the action of the compressive force.[17] For a full derivation and physical description of Eq. 1, the interested reader is directed to Concha et al.[16]

Of particular interest in the current work are the permeability and solid stress functions, $k(\phi)$ and $\sigma_e(\phi)$, respectively. To facilitate the discussion of results to follow, we briefly describe their physical significance here. The concept of permeability originated from the classic Darcy's Law relating flow rate to the pressure drop through a porous bed of particles.[18] It physically represents the ease with which a particular fluid percolates through a given porous structure and appears in the formulation empirically by the interphase momentum transfer term. For cellulose fiber suspensions, researchers represent the permeability $k(\phi)$ of the network by either a Kozeny–Carman expression, multibody drag models, or Lattice–Boltzmann simulations.[19-21] A large variation in permeability functions, which is reported in this literature, stems from the irregularity in the size and shape of the fibers and differences in their ability to absorb and retain water. Aspects of this have been addressed in the papers by Jonsson and Jonsson.[22,23] As a result, $k(\phi)$ is treated as an empirical function that must be determined experimentally for the particular suspension under study.

The solid stress function $\sigma_e(\phi)$ describes the uniaxial compression of the fiber network. In Eqs. 1–5, the solid phase is treated as an isotropic material, the shear stresses in the network are neglected, and the solid-phase stress tensor is completely characterized by $\sigma_e(\phi)$ alone. A commonly cited functional form of $\sigma_e(\phi)$ is

$$\sigma_e(\phi) = \begin{cases} 0 & : \phi \leq \phi_g \\ m(\phi^n - \phi_g^n) & : \phi > \phi_g \end{cases} \quad (6)$$

where m and n are empirical constants and ϕ_g, the gelation point, is defined as the value below which $\sigma_e(\phi)$ cannot be experimentally distinguished from zero.[3] The monotonically increasing functional form is consistent with physical intuition. Compression of the network to higher concentration is achieved by continuous increase in applied pressure. This increase grows sharply as the material becomes more compressed. It should be noted that Martinez et al.[3] measured ϕ_g experimentally. This formulation for $\sigma_e(\phi)$ neglects plastic deformation and time-dependent behavior, which are not important for our study.

From the above development, it is clear that the equations of motion do not constitute a closed system. The success of a mathematical model in this case is dependent on the accuracy of the closure equations for the permeability and solid-stress functions, which must be determined by experiment. Our objective in this paper is to do so using an iterative procedure that attempts to match experimental data to a numerical model.

This article is organized as follows. The transient settling process is explored with a new tool: positron emission tomography (PET). Here, the behavior of fluorine-18 (^{18}F)–labeled papermaking fibers settling by gravity in the midst of a suspension of nonradioactive fibers is studied using PET. We measure the concentration profile of the radioactive tracer along the sedimentation axis as a function of time. We then follow by outlining the numerical method used to solve the inverse problem, that is, to estimate $k(\phi)$ and $\sigma_e(\phi)$ by comparing the equations of motion to the experimental data.

Visualization of the Transient Settling Process

There are a number of experimental techniques currently available to visualize the settling process: light transmission,[24] X- or γ-ray, acoustics,[25,26] or nuclear magnetic resonance.[27-30] For papermaking suspensions, it is important to measure the motion of the various fiber fractions within a suspension, from low to high concentrations, to gain insight into the macroscopic properties of the suspension. The experimental measurements mentioned above are "global" in nature in that the motion of individual particles cannot be detected. Herzhaft et al.[31] recently visualized the motion of marked fibers, in a suspension of unmarked fibers made optically transparent by matching the index of refraction. Although this technique worked well with glass fibers, where all particles have similar physical properties, this technique would be difficult to use with papermaking suspensions. As a result, one objective of this paper is to develop a method to visualize the motion of the fibers in papermaking suspensions. We do so using a new tool: positron emission tomography (PET).

Suspension preparation

A suspension of thermomechanical pulp fibers in water was used in this work. Fiber-length fractions of this suspension were obtained by classification in a Bauer–McNett classifier. Fractions of various fiber lengths were collected separately and stored for further testing. Fiber length was measured for each fraction with an automated fiber length analyzer (FQA obtained

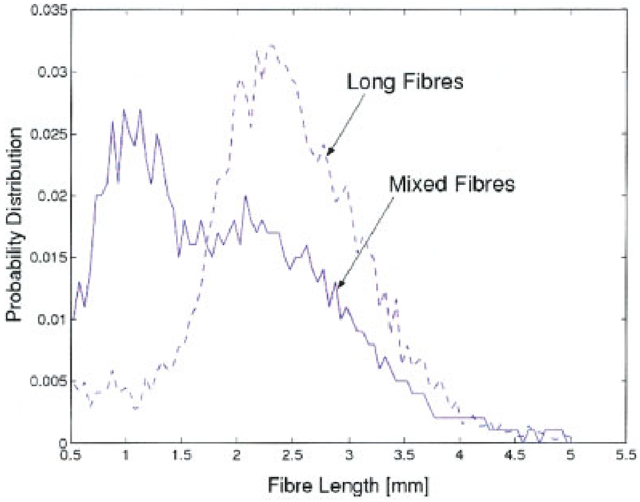

Figure 1. Fiber length distributions for the long and mixed tracers.

[Color figure can be viewed in the online issue, which is available at www.interscience.wiley.com]

from Optest.ca). Two fiber fractions were chosen for further study; we will refer to these as the "long" and "mixed" tracers. The fiber-length distributions of the tracers are shown in Figure 1. Based on the initial settling velocities reported by Marton and Robie[32] for mechanical pulp fibers, we estimate the fiber Reynolds number, defined as $lV_s\rho_f/\mu$, to be approximately 10^{-2}. Thus, the effect of inertial forces is assumed negligible for the experimental conditions tested.

The sedimentation experiments were performed in a plastic jar with a circular cross section having an inner diameter of 87 ± 1 mm. This represents a diameter that is at least $40l$, based on the long fiber fraction. This is sufficiently large to accurately measure bulk properties in the middle of the suspension. It should be noted that the plastic jar was slightly rounded at the bottom with a radius of curvature measured to be 200 mm. The suspensions filled up the jar to a height of about 159 ± 3 mm for all tests.

The settling experiments were conducted by first radioactively labeling a selected Bauer–McNett fraction of fibers with ^{18}F and reintroducing this into the original suspension. Details of the labeling procedure were previously described.[3] Briefly, the fibers were suspended in a solution of acetic acid while ^{18}F–F$_2$ was bubbled through the suspension at 10 mL/min with constant stirring. After the addition of the fluorine, the fibers were filtered and washed with distilled water. At this point the fibers were labeled with ^{18}F with a 10% yield based on the total radioactivity introduced. ^{18}F was chosen here in preference to other positron emitting tracers such as ^{15}O, ^{11}C, or ^{13}N because of its reasonably long half-life of 110 min and its reactivity with pulp fibers. Known masses of both the radioactive tracer and nonradioactive fibers were added to the sedimentation jar and the rest of the jar was filled with water. Care was taken to re-create the same fiber-length distribution for the whole-pulp suspension. Typically, 0.3 g of radioactive fibers was used for each experiment in about 2 g of total fibers. The radioactive fibers therefore represent only a small fraction of the total fibers in the system, and any potential change to the surface chemistry of the fibers arising from the labeling process is assumed to be negligible. Air was removed from the suspension by using vacuum and the suspension was mixed by rotating and tumbling the jar for about 5 min. The experiments were conducted at a concentration of 2.3 kg/m^3.

Visualization

Positron emission tomography (PET) is an imaging technique widely developed for diagnostic medicine but has recently been applied to engineering studies.[33-40] Each emitted positron annihilates with a nearby electron producing two collinear 511-keV γ-rays traveling in opposite directions. Simultaneous detection by γ-ray sensitive detectors located on either side of the system[41] defines a line close to which the radioactive decay must have occurred. By detecting many of these decays, the distribution of activity can be determined. With the tomograph used here (ECAT 958B, Siemens Medical Systems, Malvern, PA), images are scanned along 31 different parallel planes, 3.37 mm thick, to give an axial extent of about 100 mm. Each axial plane is made up 128 × 128 pixels, 2.53 mm^2.

The following imaging protocol was used for both the long and mixed fraction tests. A total of 27 images were captured over 2 h of imaging. The framing rates were as follows: four images at 15-s exposure times over the first minute; two frames with 30-s exposures over the second minute; eight images at 1-min exposure times over the next 8 min; four images at 5-min exposure times over the next 20 min; and then nine images at 10-min exposure times. After each experiment, a "transmission scan " was made to calculate the corrections for photon attenuation from the nonradioactive materials in the suspension. The transmission scan was performed after the radioisotope was allowed to decay for nearly ten half-lives.

Visualization results

The transmission scan provided the necessary calibration for calculating the true activity so that the data can be reconstructed into three-dimensional emission images as illustrated in Figure 2. Activity was then related to the mass of radioactive fibers from an independent calibration procedure.[3] In most sedimentation studies found in the literature, researchers usually assume that the spatial distribution of particles in the horizontal plane is uniform. This assumption can be verified with these images and we estimate that the variation in each horizontal plane to be nearly 17%. This estimate remains essentially constant for every time step. As a result, we represent the dynamics of the sedimentation process as vertical concentration profiles determined from averages of square subimages (46 × 46 mm), sampled from the center of the sedimenting jar. Image reconstruction and analysis were performed with MATLAB (The MathWorks, Natick, MA).

It should be noted that we are uncertain of the concentration measurement in the first few pixels near the top of the sediment. There are two phenomena that need to be considered here. It is well known that at interfaces between radioactive and nonradioactive materials, PET images appear somewhat "smeared" when reconstructed. Smearing generally occurs over two to three pixels. On the other hand, a naturally occurring concentration gradient must exist at this point as a result of polydispersity and hydrodynamic self-diffusion effects.[27] Ac-

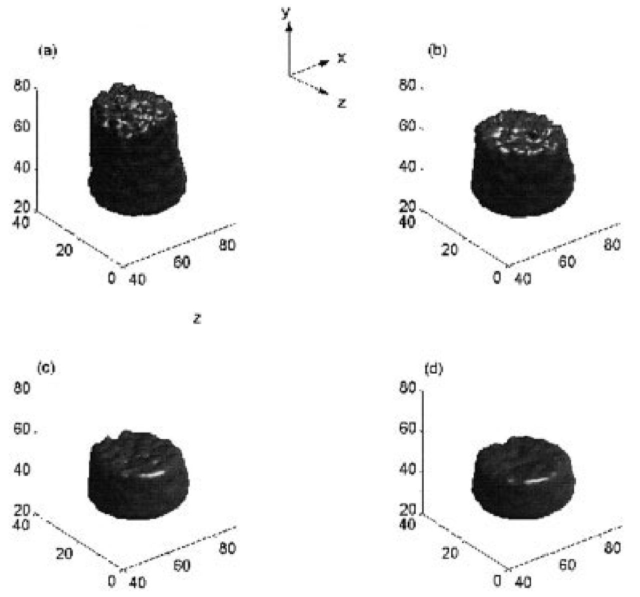

Figure 2. Three-dimensional reconstruction of the radioactivity distributions inside the settling jar at different times.

(a) t = 4, (b) t = 12, (c) t = 20, (d) t = 28 min. The axes represent the pixel positions.

curately decoupling the "smearing" from the real concentration gradient is difficult, if not impossible. In this work we do not attempt to decouple these effects but, instead, delineate the areas of uncertainty in the measured signal by the hatched lines given in Figure 3 (reproduced from Martinez et al.[3]). Only four of the 27 total profiles are plotted for clarity. In these profiles, each data point represents normalized concentration C/C_0 at a particular normalized height y/H_0. The decrease in the signal at about 5 mm from the bottom of the container reflects the fact the bottom of the jar was rounded. By integrating these curves, we find that the total radioactivity remained essentially constant for every time step. The total radioactivity, found to vary at most 4%, demonstrates the internal consistency of the measurement technique.

The form of these profiles was found to be similar for all cases tested by Martinez et al.,[3] and the time frames shown clearly illustrate the dynamics of the sedimentation process. We complement this result by reporting the height of the interface between the suspension and the clear water for both fiber fractions tested, as shown in Figure 4. We show data for only the first 30 min of the 2-h experiment because the interface height does not noticeably change beyond this point. We find that initially the interface moves downward at a constant rate as a layer of sediment builds up at the bottom of the container. We speculate that as the interface approaches the height of sediment, its rate of fall decreases until a "critical settling point" is reached when a direct interface is formed between the sediment and the nonradioactive material. At this point the sedimentation rate decreases dramatically. Further sedimentation beyond this point results solely from the consolidation of the sediment. Finally, it is interesting to note in Figure 3 that at t = 10 min a large concentration gradient is evident in the sediment. The porosity of the sediment is smallest at the bottom because the compressive force resulting from the weight of the fibers is greatest. Although network compressibility has been observed by other researchers,[12,13,42] these profiles illustrate that it leads to a very significant concentration gradient in the sediment to a degree that the use of an average sediment concentration is questionable as a means of characterizing the suspension.

It is evident from these plots that there is a higher concentration of the mixed fraction tracer than the long fraction tracer at the bottom of the settling jar. This suggests that the small particles in the mixed fraction are more mobile and network formation commences with the immobilization of the longer fibers. However, we note that the differences are quite small.

Finally, with the uncertainty in the measured interfacial heights, we found no statistical difference between the initial settling rates of the different fiber fractions, see Figure 4. This contrasts the results of Marton et al.[32] who report that long fibers settle at higher rates than shorter ones, when tested separately, that is, when the individual fiber fractions are allowed to settle by themselves. Our findings apply to settling rates of fiber fractions inside a mixture. This phenomenon

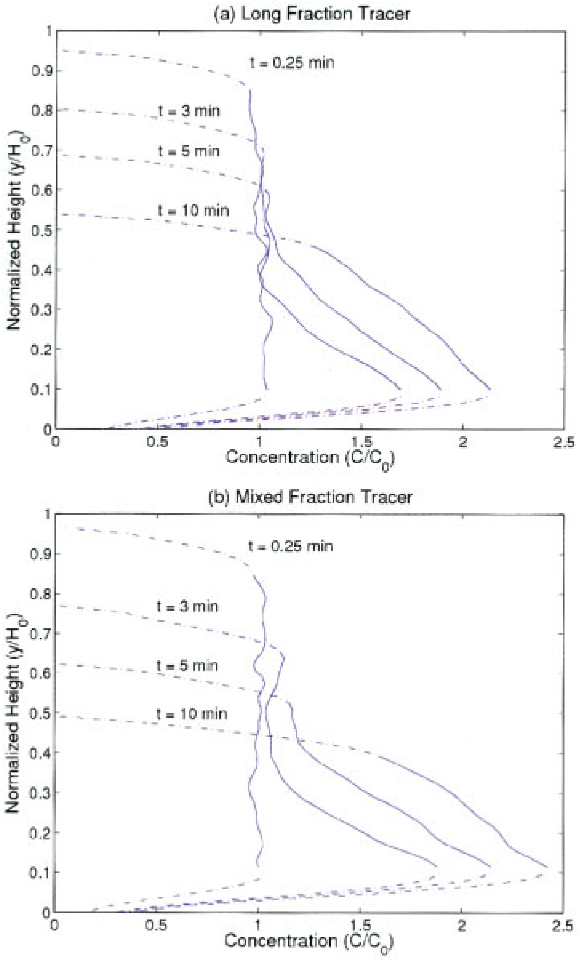

Figure 3. Concentration profiles from PET with (a) the long fraction tracer and (b) the mixed fraction tracer settling within the suspension.

For clarity, only four of the 27 images are shown in each graph. [Color figure can be viewed in the online issue, which is available at www.interscience.wiley.com]

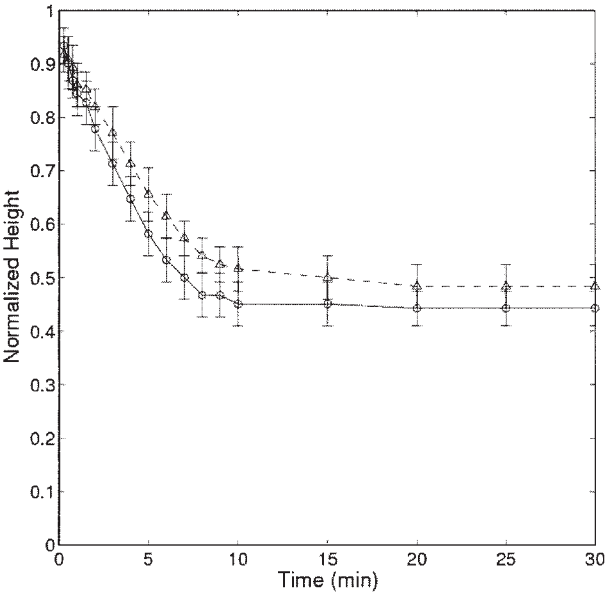

Figure 4. Movement of the interface between the radioactive tracers and the clear fluid measured as a function of time.

Each tracer is differentiated by the type of symbol used (triangle: long fibers; circle: mixed fibers). The uncertainty in the measured height of the interface is given by the error bars.

results from the fact that larger fibers are retarded to a greater extent than the smaller ones in these concentration regimes.

Estimating Permeability and Solid-Stress Functions

The previous section established the usefulness of PET to measure the evolution of the solidity profile in a settling suspension. It also showed that significant concentration gradients existed over the depth of the sediment, implying that there is no unique sedimentation concentration. To make these sediment tests useful, a method was developed to estimate $k(\phi)$ and $\sigma_e(\phi)$ from these experimental measurements. An inverse solver was used to estimate empirical parameters of the constitutive relationships by comparing the experimental data to Eqs. 1–7.

The inverse solver consisted of the following four major components. The first component was the selection of appropriate functional forms for $k(\phi)$ and $\sigma_e(\phi)$ to completely close the set of equations. In the current work, solid stress was characterized by Eq. 6, whereas permeability was modeled using the relationship

$$k(\phi) = \frac{pe^{-r\phi}}{\phi} \tag{7}$$

where p and r are empirical constants to be determined. This relationship is similar to the form reported by Koponen et al.[21] obtained from Lattice–Boltzmann simulations. With the selection of these two relationships, complete solution of Eqs. 1–7 ultimately depended on the set of four empirical parameters m, n, p, and r arising from the two constitutive functions.

The second component is the use of a "forward" finite difference solver for determining a numerical solution of Eq. 1, given a particular set of m, n, p, and r. Briefly, Eq. 1 was discretized using an explicit Euler time-advance scheme for the time derivative, a second-order three-point monotone scheme[43] for the first derivative "convective" term, and a second-order conservative approach for the second derivative "diffusive" term. For any given set of m, n, p, and r, ϕ was then determined at all spatial and temporal points of interest. A rather sophisticated discretization of the first derivative term was necessary to maintain a sharp discontinuity at the suspension–supernatant interface. Further details of the forward solver are included in the Appendix.

The third component is a simple least-squares calculation required to quantify a pointwise comparison between the experimental data obtained from PET and the calculated guess from the forward solver. The least squares calculation used was

$$S(m, n, p, r) = \sum_i \sum_j [(\phi_{\text{expt}})_j^i - (\phi_{\text{calc}})_j^i]^2 \tag{8}$$

where $(\phi_{\text{expt}})_j^i$ is the experimental solidity measured at time step i and spatial point j, $(\phi_{\text{calc}})_j^i$ is the corresponding solidity from the forward numerical solution at i and j, and S is the overall discrepancy between the experimental and numerical solutions. It is determined by summing the squares of the differences at all i and j, and is a function of the set of empirical parameters.

Finally, the fourth component of the inverse solver was the use of a minimization scheme, called Powell's method to find the minimum of S and ultimately the solution to $(\phi_{\text{calc}})_j^i$ that provides the best fit to the experimental data. Powell's method was chosen for this problem because of its robustness and relative simplicity in comparison to conjugate gradient methods, which require additional calculations for function derivatives that are often difficult and computationally expensive.[44] In the current work, the discrepancy S is a four-variable function of m, n, p, and r. Minimization of S was achieved through a series of line minimizations using the one-dimensional Brent's method along one given direction. These line minimizations were performed successively in different directions chosen for optimal efficiency, based on the detailed description provided in Press et al.[44]

Results and Discussion

For all results presented below, the numerical solutions were obtained using 201 grid points (including endpoints) with a constant time step of $\Delta t = 0.025$ s to ensure stability of the time-marching scheme for this grid spacing. This grid size was chosen to ensure proper grid convergence of the solution without being too computationally expensive. For Powell's method, all parameters were converged to an accuracy of four significant figures. This was ensured by determining through trial and error an appropriate order-of-magnitude scaling for each parameter such that the searching procedure for the optimum parameters was performed over a smaller range of values. More specifically, scaling parameters for m, n, p, and r were 10^8, 10^0, 10^{-11}, and 10^1, respectively. Powell's method was then reduced to optimizing coefficients for m, n, p, and r that lay within the range of about 1 to 100, which significantly improved the performance of the algorithm. Note that without

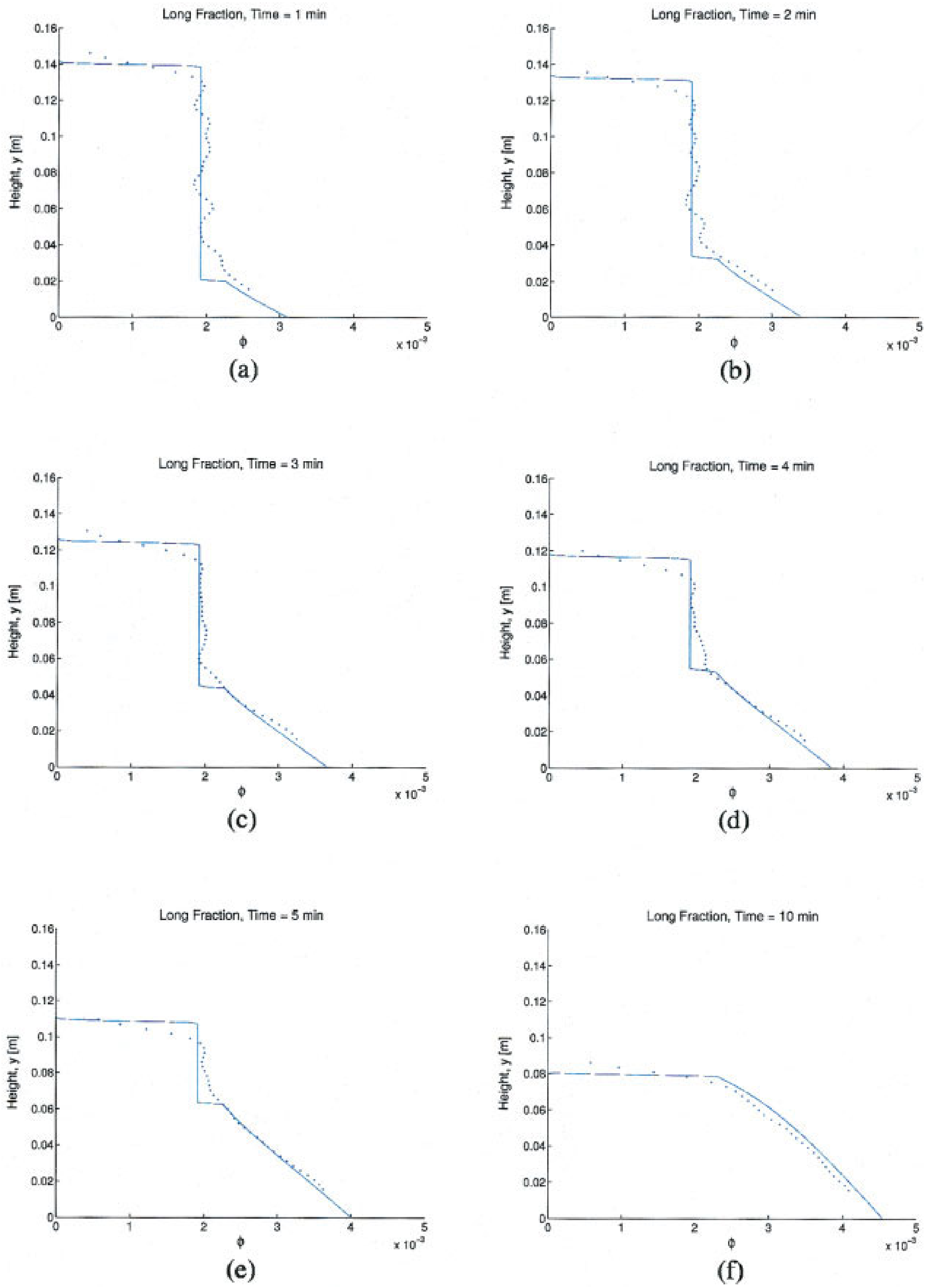

(a) (b) (c) (d) (e) (f)

Figure 5. Comparison plots of the long fraction tracer, for selected times from t = 1 min to t = 10 min.

[Color figure can be viewed in the online issue, which is available at www.interscience.wiley.com]

the scaling parameters, the expected optimum values for m, n, p, and r would span a range of 10^{19}.

The best fits of the model to the experimental data for the long and mixed fractions are shown in Figures 5 and 6 respectively. The dots represent the experimental results obtained from PET and the lines represent the numerical solution obtained from the forward solver. The first observation that can be made from these figures is the model fits the data reasonably well, given that the correlation coefficient was found to be $r^2 = 0.94$ for the long fraction and $r^2 = 0.96$ for the mixed fraction. Estimates of the parameters m, n, p, and r are shown in Table 1. Because of the uncertainty with experimental data, these parameters are reported with only two significant digits, even though the convergence criterion for Powell's method was for four significant digits. In general, similar values were obtained for both trials, with the values of m and p being slightly

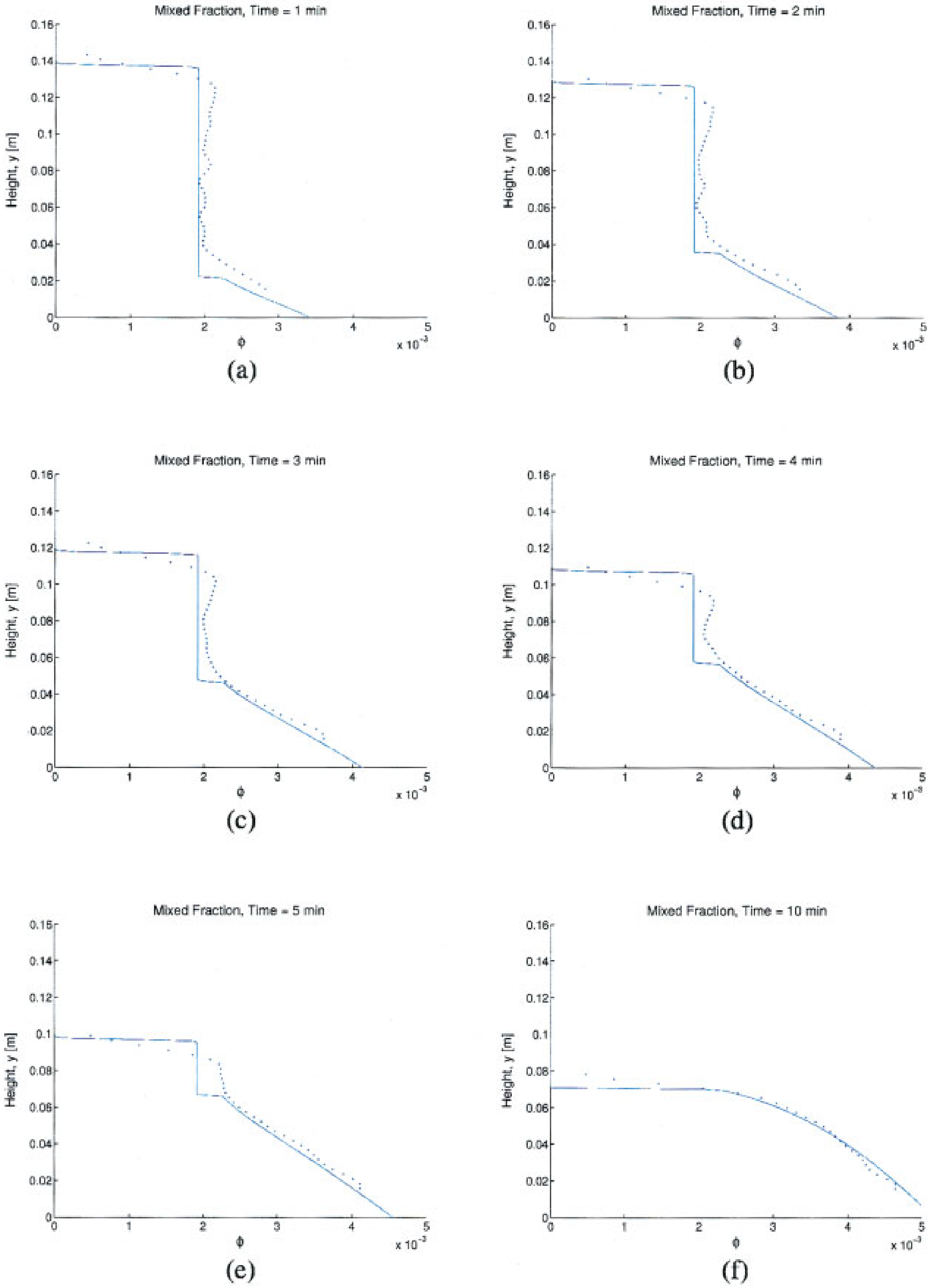

(a) (b) (c) (d) (e) (f)

Figure 6. Comparison plots of the mixed fraction tracer, for selected times from t = 1 min to t = 10 min.

[Color figure can be viewed in the online issue, which is available at www.interscience.wiley.com]

different. The variation in these parameters was enough to characterize the major differences in settling rates and networking behavior between the two fractions.

Equation 7 was found to be the best choice for the functional form of $k(\phi)$. An exponential form $k(\phi) = pe^{-r\phi}$, used by Koponen et al.[21] for modeling the permeability of three-dimensional random fiber webs, was also tested, but was found to be unsuccessful in matching the experimental data. The exponen-

Table 1. Optimal Parameters Obtained for the Long and Mixed Tracers

Parameter	Long Fraction Tracer	Mixed Fraction Tracer
m	11×10^{8}	7.2×10^{8}
n	4.0	4.0
p	1.4×10^{-10}	1.8×10^{-10}
r	4.0×10^{2}	4.0×10^{2}

tial form fitted the data from Koponen et al. for the range $0.2 < \phi < 0.6$. In our case, however, where much lower solidities of $\phi < 0.005$ were studied, the exponential form was unable to generate a sharp discontinuity in the numerical solution at the suspension–supernatant interface. Because other forms cited in the literature (including the Kozeny–Carman relationship) incorporated a factor of $1/\phi$ that allowed for infinite permeability as solidity approached zero,[45] Eq. 7 essentially combined this feature with the exponential form. This provided a good fit with the experimental data and also produced a sufficiently sharp discontinuity at the interface.

As shown in Figures 5 and 6, there were features of the experimental data that were not captured by the model. As discussed previously, there was uncertainty in the experimental measurements at the interface between the suspension and the clear fluid. As a result we were uncertain of the concentration profile in this region. This also led to an uncertainty in mass because it was difficult to accurately integrate the area under the experimental curves. Thus, a small error in mass conservation of nearly 4% was found over the time of settling. Further, the experimental data were volume-averaged such that small-scale features were filtered. Consequently, we cannot expect the experimental data to fit the model at the sharp discontinuities, either at the interface or between the free-settling zone and the networked region. Note that the horizontal line between the free-settling suspension region and the concentrated network represents a discontinuity and has physical significance. The solidity in the free-settling zone remains constant at the initial solidity, $\phi = \phi_0$. However, by definition, the top of the network must reach the gelation point ϕ_g. This difference creates the discontinuity in the numerical solution.

Finally, in most trials conducted, fluctuations in the concentration profile were evident in the data near the start of the experiment. An example of this can be seen in the plots at $t = 1$ min in Figures 5 and 6. This phenomenon was also evident in the data reported by Martinez et al.[3] Although we do not have an explanation for this phenomenon, Herzhaft et al.[31] reported horizontal and vertical velocity fluctuations in their sedimentation experiments with both dilute and semidilute suspensions of glass rods. These velocity fluctuations very likely led to the oscillatory nature observed in our concentration profiles. Unfortunately, such a phenomenon cannot be captured by the model and may indicate a limitation in the model's usefulness.

Conclusions

In this article, we studied the sedimentation of papermaking fibers in semidilute suspensions to determine the permeability and solid-stress functions. To do so, a novel approach using positron emission tomography was used to measure the evolution of the solidity profile. Here ^{18}F-labeled fibers were used as tracer particles. With this technique, we were able to confirm the existence of a substantial concentration gradient in the sediment layer. This is a significant finding because it shows that an average sediment concentration cannot be used as a means of characterizing a fiber suspension. We subsequently compared the experimental data obtained from PET to the Eulerian volume-averaged two-phase flow equations, with assumed relationships for the solid-stress and permeability functions (Eqs. 6 and 7, respectively). Estimated values for the empirical constants m, n, p, and r were obtained successfully using an "inverse" solver that consisted of a forward finite difference solver, a least-squares fit calculation, and Powell's method for minimization. Good agreement was found between the experimental data and the numerical model using the specified functional forms and the fitted parameters. This general approach can be used either to examine the networking characteristics of different mixed suspensions of fibers or to investigate other possible functional forms for solid stress and permeability.

Acknowledgments

The authors thank Dr. Ian Frigaard for help in numerical aspects of this work. We also thank all the reviewers for insightful comments and helpful suggestions throughout the review process. We gratefully acknowledge financial support of TRIUMF through its Life Sciences program, Forest Renewal BC through the Advanced Papermaking Initiative, and the Natural Sciences and Engineering Research Council of Canada.

Literature Cited

1. Nazhad MM, Harris EJ, Dodson CTJ, Kerekes RJ. Influence of formation on tensile strength of papers made from mechanical pulps. *TAPPI J.* 2000;83:63-63.
2. Kulikova YY, Schaepe MK, Robbins WB. Assessment of the influence of paper formation on the fluorescence contribution to brightness. *Color Res Appl.* 1995;20:87-92.
3. Martinez DM, Buckley K, Jivan S, Lindstrom A. Characterizing the mobility of papermaking fibres during sedimentation. *Transactions of the 12th Fundamental Research Symposium, Oxford, 2001*. Oxford, UK: Oxford Univ. Press; 2001:225-254.
4. Kerekes RJ, Soszynski RM, Tam Doo PA. The flocculation of pulp fibres. *Transactions of the 8th Fundamental Research Symposium, Oxford, UK*. Oxford, UK: Oxford Univ. Press; 1985:265-310.
5. Mackaplow MB, Shaqfeh ESG. A numerical study of the sedimentation of fibre suspensions. *J Fluid Mech.* 1998;376:149-182.
6. Koch DL, Shaqfeh ESG. The instability of a dispersion of sedimenting spheroids. *J Fluid Mech.* 1989;209:521-542.
7. Turney MA, Cheung MK, Powell RL, McCarthy MJ. Hindered settling of rod-like particles measured with magnetic-resonance-imaging. *AIChE J.* 1995;41:251-257.
8. Claeys IL, Brady JF. Suspensions of prolate spheroids in Stokes flow. Part 3. Hydrodynamic transport properties of crystalline dispersions. *J Fluid Mech.* 1993;251:479-500.
9. Kuusela E, Hofler K, Schwarzer S. Computation of particle settling speed and orientation distribution in suspensions of prolate spheroids. *J Eng Math.* 2001;41:221-235.
10. Butler JE, Shaqfeh ESG. Dynamic simulations of the inhomogeneous sedimentation of rigid fibres. *J Fluid Mech.* 2002;468:205-237.
11. Saintillan D, Darve E, Shaqfeh ESG. A smooth particle-mesh Ewald algorithm for Stokes suspension simulations: The sedimentation of fibers. *Phys Fluids.* 2005;17:033301.
12. Ingmanson WL, Andrews BD, Johnson RC. Internal pressure distributions in compressible mats under fluid stress. *TAPPI J.* 1959;42: 840-849.
13. Meyer H. A filtration theory for compressible fibrous beds formed from dilute suspensions. *TAPPI J.* 1962;45:296-310.
14. Ystrom J. *On the Numerical Modeling of Concentrated Suspensions and of Viscoelastic Fluids*. PhD Thesis. Stockholm, Sweden: Royal Institute of Technology (KTH); 1996.
15. Enwald H, Peirano E, Almstedt AE. Eulerian two-phase flow theory applied to fluidization. *Int J Multiphase Flow.* 1996;22:21-66.
16. Concha F, Bustos MC, Barrientos A. Phenomenological theory of sedimentation. In: Tory EM, ed. *Sedimentation of Small Particles in a Viscous Fluid*, Southampton, UK: Computational Mechanics Publications, 1996:51-96.
17. Kirmanen J, Kataja M, Timonen J. Stress balance in soft porous-media. *Appl Phys Lett.* 1994;64:2605-2607.
18. Scheidegger AE. *The Physics of Flow Through Porous Media*. Toronto, Canada: University of Toronto Press; 1974.
19. Vomhoff H. *Dynamic Compressibility of Water Saturated Networks*

and Influence of Local Stress Variations in Wet Pressing. PhD Thesis. Stockholm, Sweden: Royal Institute of Technology (KTH); 1998.

20. Koponen A, Kataja M, Timonen J. Permeability and effective porosity of porous media. *Phys Rev E.* 1997;56:3319-3325.
21. Koponen A, Kandhai D, Hellen E, Alava M, Hoekstra A, Kataja M, Niskanen K, Sloot P, Timonen J. Permeability of three-dimensional random fiber webs. *Phys Rev Lett.* 1998;80:716-719.
22. Jonsson KAS, Jonsson BTL. Fluid-flow in compressible porous-media. 1. Steady-state conditions. *AIChE J.* 1992;38:1340-1348.
23. Jonsson KAS, Jonsson BTL. Fluid-flow in compressible porous-media. 2. Dynamic behavior. *AIChE J.* 1992;38:1349-1356.
24. Davis RH, Birdsell KH. Hindered settling of semidilute monodisperse and polydisperse suspensions. *AIChE J.* 1988;34:123-129.
25. Bacri JC, Hoyos M, Rakotomalala N, Salin D, Bourlion M. Ultrasonic diagnostic in porous-media and suspensions. *J Phys III.* 1991;1:1455-1466.
26. Martin J, Rakotomalala N, Salin D. Accurate determination of the sedimentation flux of concentrated suspensions. *Phys Fluids.* 1995;7:2510-2512.
27. Turney MA, Cheung MK, McCarthy MJ, Powell RL. Magnetic-resonance-imaging study of sedimenting suspensions of noncolloidal spheres. *Phys Fluids.* 1995;7:904-911.
28. Bobroff S, Phillips RJ. Nuclear magnetic imaging investigation of sedimentation of concentrated suspensions in non-Newtonian fluids. *J Rheol.* 1998;42:1419-1436.
29. Lee S, Jang Y, Choi C, Lee T. Combined effect of sedimentation-velocity fluctuation and self-sharpening on interface broadening. *Phys Fluids A: Fluid Dyn.* 1992;4:2601-2606.
30. Cheung MK, Powell RL, McCarthy MJ. Sedimentation of noncolloidal bidisperse suspensions. *AIChE J.* 1996;42:271-276.
31. Herzhaft B, Guazzelli E. Experimental study of the sedimentation of dilute and semi-dilute suspensions of fibres. *J Fluid Mech.* 1999;384:133-158.
32. Marton R, Robie JD. Characterization of mechanical pulps by a settling technique. *TAPPI J.* 1969;52:2400-2406.
33. Bridgwater J, Broadbent CJ, Parker DJ. Study of the influence of blade speed on the performance of a powder mixer using positron emission particle tracking. *Chem Eng Res Des.* 1993;71:675-681.
34. Broadbent CJ, Bridgwater J, Parker DJ, Keningley ST, Knight PA. Phenomenological study of a batch mixer using a positron camera. *Powder Technol.* 1993;76:317-329.
35. Broadbent CJ, Bridgwater J, Parker DJ. The effect of fill level on powder mixer performance using a positron camera. *Chem Eng J/Biochem Eng J.* 1995;56:119-125.
36. Garncarek Z, Przybylski L, Botterill JSM, Bridgwater J, Broadbent CJ. A measure of the degree of inhomogeneity in a distribution and its application in characterizing the particle circulation in a fluidized-bed. *Powder Technol.* 1994;80:221-225.
37. Snieders FF, Hoffmann AC, Cheesman D, Yates JG, Stein M, Seville JPK. The dynamics of large particles in a four-compartment interconnected fluidized bed. *Powder Technol.* 1999;101:229-239.
38. Khalili A, Basu AJ, Pietrzyk U. Flow visualization in porous media via positron emission tomography. *Phys Fluids.* 1998;10:1031-1033.
39. Khalili A, Basu AJ, Pietrzyk U, Raffel M. An experimental study of recirculating flow through fluid-sediment interfaces. *J Fluid Mech.* 1999;383:229-247.
40. Hoff WD, Wilson MA, Benton DM, Hawkesworth MR, Parker DJ, Fowles P. The use of positron emission tomography to monitor unsaturated water flow within porous construction materials. *J Mater Sci Lett.* 1996;15:1101-1104.
41. Stellema CS, Vlek J, Mudde RF, de Goeij JJM, van den Bleek CM. Development of an improved positron emission particle tracking system. *Nucl Instrum Methods Phys Res A: Accel Spectrom Detect Assoc Equip.* 1998;404:334-348.
42. Robertson AA, Mason SG. Specific surface of cellulose fibres by the liquid permeability method. *Pulp Paper Mag Canada.* 1949;50:103-110.
43. Evje S, Karlsen KH. Monotone difference approximations of BV solutions to degenerate convection-diffusion equations. *SIAM J Numer Anal.* 2000;37:1838-1860.
44. Press WH, Teukolsky SA, Vetterling WT, Flannery BP. *Numerical Recipes in C.* Cambridge, UK: Cambridge Univ. Press, 1992:394-455.
45. Happel J. Viscous flow relative to arrays of cylinders. *AIChE J.* 1959;5:174-177.
46. Burger R, Evje S, Karlsen KH, Lie KA. Numerical methods for the simulation of the settling of flocculated suspensions. *Chem Eng J.* 2000;80:91-104.

Appendix

Examination of Eq. 1 reveals that it is a mixed hyperbolic–parabolic equation because of the piecewise nature of the solid stress function. A suitable discretization must therefore be chosen to deal with the inherent difficulties of this equation. After carefully reviewing the literature, we chose to adopt a numerical scheme outlined in Bürger et al.[46] A summary of this method is given below. To aid in this summary, we define the different derivative terms in Eq. 1 as such: the first term is defined as the "time derivative"; the second term as the "convective term"; and the third term as the "diffusive term."

First, consider the discretization of the convective term. Here, we use a second-order three-point monotone scheme, which is described in detail by Evje and Karlsen.[43] If we define $H(\phi)$ as

$$H(\phi) = -\frac{\Delta\rho g\phi k(\phi)}{\mu} \tag{A1}$$

the proposed scheme results in the following discretization:

$$\frac{\partial}{\partial y} H(\phi) \approx \frac{F(\phi_j^R, \phi_{j+1}^L) - F(\phi_{j-1}^R, \phi_j^L)}{\Delta y} \tag{A2}$$

where F is the general upwind flux function, defined as

$$F(\phi_j^n, \phi_{j+1}^n) = H^+(\phi_j^n) + H^-(\phi_{j+1}^n) \tag{A3}$$

$$H^+(\phi) = H(0) + \int_0^\phi \max[H'(s), 0]ds \tag{A4}$$

$$H^-(\phi) = \int_0^\phi \min[H'(s), 0]ds \tag{A5}$$

The inputs of F in Eq. A2, ϕ_j^L and ϕ_j^R, which are the left and right extrapolated values of the general solution point ϕ_j^n, are evaluated as

$$\phi_j^L = \phi_j^n - s_j^n \frac{\Delta y}{2} \tag{A6}$$

$$\phi_j^R = \phi_j^n + s_j^n \frac{\Delta y}{2} \tag{A7}$$

given

$$s_j^n = s\left(\frac{\phi_j^n - \phi_{j-1}^n}{\Delta y}, \frac{\phi_{j+1}^n - \phi_j^n}{\Delta y}\right) \tag{A8}$$

and

$$s(a, b) = \frac{1}{2}[\operatorname{sgn}(a) + \operatorname{sgn}(b)]\min(|a|, |b|) \tag{A9}$$

where $s(a, b)$ is the minmod limiter. Note that the superscripts L and R merely indicate the direction of the extrapolation (left or right); that is, these extrapolated values are still evaluated at time step n.

For the diffusive term, if we define $P(\phi)$ as

$$P(\phi) = -\frac{\phi k(\phi)\sigma_e'(\phi)}{\mu} \tag{A10}$$

the term can be discretized using the conservative approach, that is,

$$\frac{\partial}{\partial y}\left(P(\phi)\frac{\partial \phi}{\partial y}\right) = \frac{\partial^2}{\partial y^2}A(\phi) \approx \frac{A(\phi_{j-1}^n) - 2A(\phi_j^n) + A(\phi_{j+1}^n)}{(\Delta y)^2} \tag{A11}$$

where

$$A(\phi) = \int_0^\phi P(\eta)d\eta \tag{A12}$$

represents the antiderivative of the nonlinear function $P(\phi)$.

When Eqs. A2 and A11 are implemented with an explicit Euler time-advance scheme for the time derivative term, the overall discretization of Eq. 1 becomes

$$\frac{\phi_j^{n+1} - \phi_j^n}{\Delta t} + \frac{F(\phi_j^R, \phi_{j+1}^L) - F(\phi_{j-1}^R, \phi_j^L)}{\Delta y} = \frac{A(\phi_{j-1}^n) - 2A(\phi_j^n) + A(\phi_{j+1}^n)}{(\Delta y)^2} \tag{A13}$$

which can be solved by marching the solution from n to $n + 1$. The algorithm was implemented using C. The code was then validated with a simple analytical diffusion–convection problem as well as with results from Bürger et al.[46]

Manuscript received Aug. 22, 2005, and revision received Apr. 21, 2006.